2014 Canada-China Conference on Advanced Reactor Development (CCCARD-2014)
Niagara Falls Marriott Fallsview Hotel & Spa, Niagara Falls, Ontario Canada, April 27-30, 2014.

CCCARD2014-027

Effect of Thermal Ageing on the Corrosion Resistance of Stainless Steel Type 316L Exposed in Supercritical Water

Y. Jiao[1], J. Kish[1], W. Zheng[2], D. Guzonas[3], W. Cook[4],
[1] McMaster University, Hamilton, Ontario, Canada
[2] CanmetMATERIALS, Hamilton, Ontario, Canada
[3] Atomic Energy of Canada Limited, Chalk River, Ontario, Canada
[4] University of New Brunswick, Fredericton, New Brunswick, Canada
jiaoyn@mcmaster.ca, kishjr@mcmaster.ca, wenyue.zheng@nrcan.rncan.gc.ca,
guzonasd@aecl.ca, wcook@unb.ca

Abstract

The tendency for intermetallic precipitates to form in austenitic stainless steel during prolonged exposure at the expected operating temperature of the fuel cladding in the Canadian supercritical water reactor (SCWR) concept represents a possible serious threat to the intrinsic in-service corrosion performance of the candidate alloy. The objective of this study was to better understand the extent to which a thermally-aged microstructure affects the mode and extent of corrosion exhibited by Type 316L stainless steel exposed in 25 MPa supercritical water (SCW) at 550 °C for 500 h. Mechanically-abraded samples were exposed in an as-received and thermally-aged condition. Thermal ageing conducted at 815 °C (peak fuel cladding temperature expected) for 1000 h was found to produce a discontinuous network of the carbide ($M_{23}C_6$), chi (χ), laves (η) and sigma (σ) phases. The similar weight gain and oxide scale structure, composition and thickness suggested that the thermally-aged condition does not have a marked influence on the corrosion resistance.

Keywords: Stainless Steel, Thermal Ageing, Precipitates, Oxide, Supercritical Water, Corrosion

1. Introduction

A large number of corrosion screening tests have been performed in recent years to identify candidate fuel cladding materials for supercritical water reactor (SCWR) designs [1-7]. Austenitic stainless steels have received plenty of attention due to their corrosion resistance and relative radiation resistance compared to Ni-based alloys. For example, in the Japanese SCWR research programs modified versions of Type 310S stainless steels have been proposed as candidate alloys from which to fabricate fuel cladding in a pressure-vessel SCWR concept [6]. The corrosion resistance of stainless steel relies on the formation of a protective oxide scale. For 18 wt.% Cr-containing stainless steels (Type 304L/316L) the oxide scale has been reported to typically consist of a less-protective outer magnetite (Fe_3O_4) layer residing on top of a more-protective inner Fe-Cr spinel ($FeCr_2O_4$) layer [3,8]. Modifying the near surface grain structure

through cold working, as first reported many years ago [9], has a significant beneficial influence on the corrosion resistance of Type 316L in 25 MPa SCW [10,11]. This is believed to result from the enhanced Cr diffusion to the surface through the increased grain boundary area and dislocations promoting the formation of a more-protective, continuous inner Cr-rich oxide layer.

Despite the current state of knowledge, a key gap exists: namely the possible effect on the corrosion resistance of a slowly evolving microstructure due to thermal ageing. For the most part, studies reporting on the corrosion resistance of stainless steels exposed in SCW have been conducted using samples in the as-received condition (typically mill-annealed), without much consideration of the microstructure degradation that has occurred during testing at the high temperatures. Short term thermal ageing is well known to "sensitize" the microstructure of 300 series stainless steel in which Cr-rich carbide (such as $M_{23}C_6$) precipitates form on the grain boundaries, rendering the grain boundary region more susceptible [20]. Other intermetallic precipitates such as the chi (χ), laves (η) and sigma (σ) phases take longer time to form [12-15], and their effect on the corrosion resistance of stainless steel in SCW has received essentially no attention.

This study was conducted to evaluate the influence of thermal ageing on the corrosion resistance of Type 316L stainless steel exposed in SCW. This was achieved by comparing the weight gain and resultant oxide scale structure, composition and thickness formed on samples exposed in the as-received (mill annealed) and thermally-aged condition. Thermal ageing was conducted for 1000 h at 815 ℃ to precipitate the carbide ($M_{23}C_6$), chi (χ), laves (η) and sigma (σ) phases. The pre-aged samples were then exposed to 25 MPa SCW at 550 ℃ (initially with 8 ppm dissolved oxygen) for 500 h in a static autoclave. The mode and extent of corrosion that occurred was characterized using electron microscopy.

2. Experimental methods

Rectangular (20 × 10 × 1 mm) samples were prepared from a commercial Type 316L stainless steel rod (24 mm diameter) provided in the mill-annealed condition. The chemical composition was analysed using ICP-OES (Varian Spectrometer) and combustion analysis (LECO CS230). The results are shown in Table 1. A small (2 mm diameter) hole was drilled into each sample near the top to facilitate mounting on a coupon tree. A subset of these samples were sealed in a nitrogen gas purged quartz tube and thermally-aged for a 1000 h at 815 °C to precipitate all of the major intermetallic phases: $M_{23}C_6$, χ, η and σ phases. The temperature was selected to be as close to the maximum fuel cladding temperature of 825 °C expected in the Canadian SCWR design concept, but still allowing for the sequential formation of each major intermetallic precipitate type. The time-temperature-precipitation (TTP) diagram published for Type 316L stainless steel by A. Kriaa et al. [16] was used to select the appropriate temperature for this purpose. Upon removal from the furnace, the thermally-aged samples were cooled to room temperature while still sealed in the nitrogen-purged quartz tube. A set of four samples in both the as-received and thermally-aged condition were mechanically abraded to a 800 grit surface finish using SiC abrasive papers with water as a lubricant, rinsed in acetone using an ultrasonic bath and weighed prior to testing.

Table 1 Chemical composition (wt.%) of the Type 316L rod used in this study.

Cr	Ni	Mo	Mn	Si	P	S	C	Fe
16.3	10.2	2.1	1.6	0.24	0.04	0.03	0.02	Bal.

A static autoclave testing facility (CanmetMATERIALS) was used to expose a set of four samples each in the as-received and thermally-aged condition in 25 MPa SCW at 550 ℃. The exposure time was limited to just 500 h in order to prevent additional intermetallic precipitation from forming during the exposure. The deionized water used for testing had an initial dissolved oxygen concentration of 8 ppm. No attempt was made to maintain this concentration during the 500 h exposure. Both sets of samples were suspended on the same coupon tree. The test was not interrupted to facilitate multiple weight change measurements as a function of exposure time.

Prior to exposure, the microstructure of the as-received and thermally-aged material was examined in cross-section using light optical microscopy, scanning electron microscopy (SEM), and transmission microscopy (TEM); the latter two were coupled with energy dispersive X-ray spectroscopy (EDS). The sample was subsequently cold-mounted in cross-section using standard metallographic techniques and polished to a 1 μm finish. Chemical etching was conducted by contacting the polished surfaces with an acetic acid-glycerine mixture for 40 s. The SEM examination was performed using a JEOL JSM-7000F microscope equipped with a Schottky Field Emission Gun (FEG) filament and an integrated Oxford Synergy system with INCA EDS X-ray micro-analysis using an accelerating voltage of 10 kV and a working distance of 10 mm. The TEM examination was performed using JEOL 2010F TEM/STEM equipped with an Oxford Instruments EDS analyser using an accelerating voltage of 200 kV. TEM samples were prepared by mechanically abrading the original sample to a thickness of 80 μm using SiC paper and water as a lubricant. Small foils were then punched out of the thinned samples and subsequently electrochemically polished in a perchlorate acid (10%)-methanol (90%) solution at -50 ºC to create a small hole in the thin foil. Randomly selected intermetallic precipitates were identified by comparing the elemental composition determined by EDS analyses in both SEM and TEM mode with those published using the same techniques [12-15]. X-ray diffraction (XRD) after a bulk extraction was also used to help identify the intermetallic precipitates that were present after thermal ageing. The bulk extraction was carried out in a hydrochloric acid (10%)-methanol (90%) solution. X-ray diffraction patterns of the extracted powder were collected using an X-ray powder diffractometer (Bruker 8D Advanced) operated with a Cu $k_{\alpha 1}$ radiation source.

After exposure, the set of samples in the as-received and thermally-aged condition were photographed and then re-weighed. One sample from each set was selected for a more detailed examination using electron microscopy of the oxide scale formed. A plan view examination of the oxide scale was conducted first using SEM (JEOL JSM-7000F) operated with an accelerating voltage of 10 kV and a working distance of 10 mm. The sample was subsequently cold-mounted in cross-section using standard metallographic techniques and polished to a 1 μm finish. SEM (JEOL JSM-7000F) operated with an accelerating voltage of 10 kV and a working distance of 10 mm was then used again to examine the oxide scale in cross-section.

3. Results

Figure 1 shows the microstructure of the as-received and thermally-aged material as revealed using light optical microscopy. The as-received (mill-annealed) material exhibited expected features, namely coarse-grain structure with some twinning and MnS inclusions (verified by SEM-EDS). The thermally-aged material exhibited similar features, but with significant intermetallic precipitation both within the grains and on the grain boundaries. The precipitation was discontinuous in both the grains and grain boundaries. Both materials had a similar average grain size number (ASTM E1382): 9.0 for the as-received material and 9.5 for the thermal-aged material. This suggests that the prolonged thermal ageing treatment (1000 h at 815 ºC) did not induce any significant grain growth.

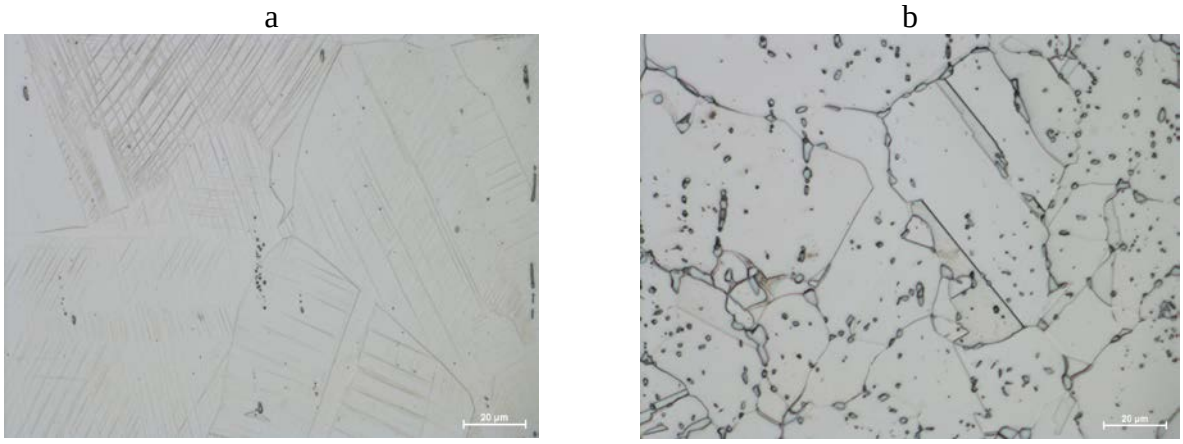

Figure 1 Light optical image of the (a) as-received (mill-annealed) material and (b) thermally-aged (1000 h at 815 ºC) material.

Figure 2 shows a typical result of the intermetallic precipitate characterization conducted using SEM-EDS and TEM-EDS. Both the EDS spot analysis (SEM) and line analysis (TEM) readily revealed the alloying elements that were enriched relative to the matrix in each case. More confidence was placed in the TEM-EDS analysis since the interaction volume is significantly less for TEM-EDS than it is for SEM-EDS. This helps to minimize the concentration dilution effect that the matrix can have on the interaction volume. The TEM-EDS line analysis clearly revealed that no obvious Cr-depletion was present adjacent the intermetallic precipitate. Thus, it appears as though the thermally ageing at such a high temperature (815 ºC) for a prolonged time (1000 h) was sufficient to ensure Cr supply in the vicinity that developed during the nucleation of such precipitates.

The XRD diffraction pattern of bulk extracted precipitates acquired from a sample in the thermally-aged condition is shown in Figure 3. Distinct peaks of the $M_{23}C_6$, χ, η and σ phases were observed. Of these phases, the χ and σ phases were dominant. Therefore, the thermal ageing heat treatment was successful in producing all of the expected major intermetallic precipitates. A summary of the intermetallic precipitates detected in the as-received and thermally-aged condition using electron microscopy and XRD techniques is provided in Table 2. A more

detailed analysis of the precipitation sequence (not reported herein) revealed that the intermetallic precipitates tended to form first on the grain boundaries and then within the matrix grains as the ageing time increased from 1 h to 1000 h.

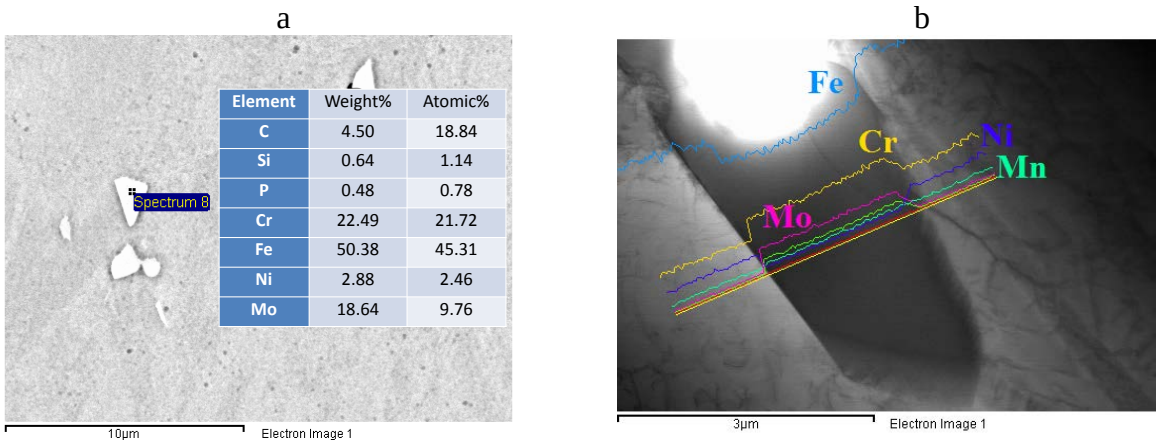

Figure 2 Electron microscopy images and EDS analyses of intermetallic precipitates found in the thermally-aged (1000 h at 815 ºC) material; (a) SEM-EDS and (b) TEM-EDS.

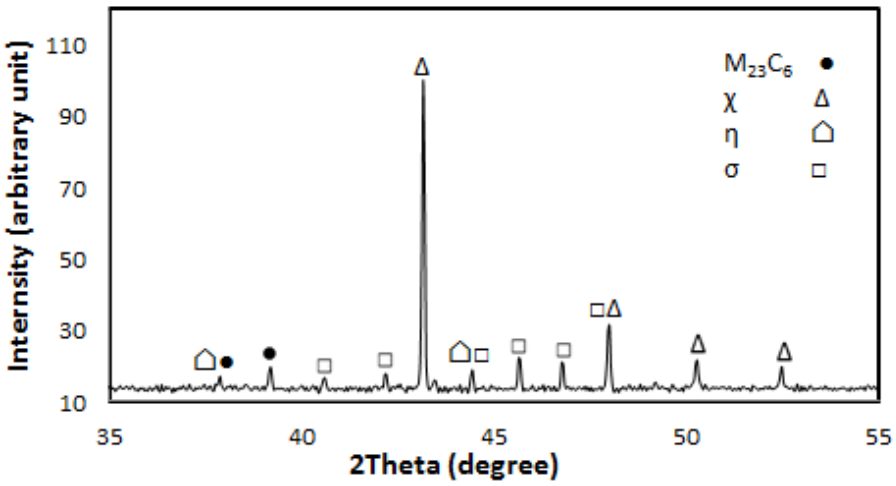

Figure 3 XRD pattern of bulk extracted precipitates.

Table 2 Summary of intermetallic precipitates detected.

Condition	SEM-EDS		TEM-EDS		XRD
	Grain	Boundary	Grain	Boundary	
As-Received	None Observed	None Observed	$M_{23}C_6$	$M_{23}C_6$	Not Analyzed
Thermally-Aged	$\chi + \sigma$	$\chi + \sigma$	$M_{23}C_6 + \chi + \sigma$	$M_{23}C_6 + \chi + \sigma$	$M_{23}C_6 + \chi + \eta + \sigma$

Figure 4 compares the average weight gain that was measured after the 500 h exposure for the set of four samples exposed in the as-received and thermally-aged condition. The "error bars" superimposed onto the chart mark the highest and lowest value recorded for each set of four samples; indicating the spread in the data. Although the average weight gain exhibited by the thermally-aged material was somewhat higher relative to that recorded for the as-received material, it was within the range of the spread associated with the as-received sample set. Based on this observation, it appears as though thermal ageing did not have a marked influence on the weight gain during the relatively short 500 h exposure. The average weight gain values do agree well with the values reported for Type 316L by Teysseyre and Was [3].

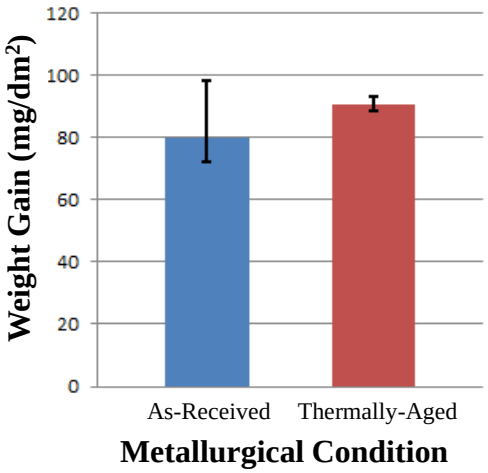

Figure 5. Weight gain of the as-received and thermally-aged material exposed.

Figure 6 shows a secondary electron image of the surface (in plan view) of an exposed sample in the as-received and thermally-aged condition. A similar surface morphology was observed on both samples: both were covered with a scale that exhibited a relatively compact plate-like granular morphology. Coarse particles were observed to be residing on top of a layer of fine particles. Significant porosity and cracking was not evident within the scale formed on either sample.

Figure 7 shows a secondary electron image and associated EDS (SEM) line analysis conducted across the oxide scale/alloy interface of an exposed sample in the as-received and thermally-aged condition. A bi-layer scale had formed in each case, consisting of a more homogeneous outer layer residing on top of a more heterogeneous inner layer. The heterogeneity in this case refers to the darker areas present the inner layer; observed more so at the scale/alloy interface than at the inner/outer layer interface. Based on the EDS line scan analysis, the inner oxide layer formed on samples with both metallurgical conditions was enriched in Cr and depleted in Fe relative to the alloy, and enriched in O. In contrast, the outer oxide layer was enriched in Fe and depleted in Cr relative to the alloy, and enriched in O. Ni was found to be somewhat enriched at the oxide scale/alloy interface. Although not reported here, XRD analysis of the oxide scale formed on an exposed sample in both metallurgical conditions showed that the scale was comprised of

crystalline magnetite (Fe_3O_4) and Fe-Cr spinel ($FeCr_2O_4$). Comparing the XRD results with the EDS line analysis results, the inner and outer layers were most likely $FeCr_2O_4$ and Fe_3O_4 respectively. This finding agrees well with the oxide scale structure and chemistry reported in the literature for Type 316L stainless steel exposed in SCW [3,8].

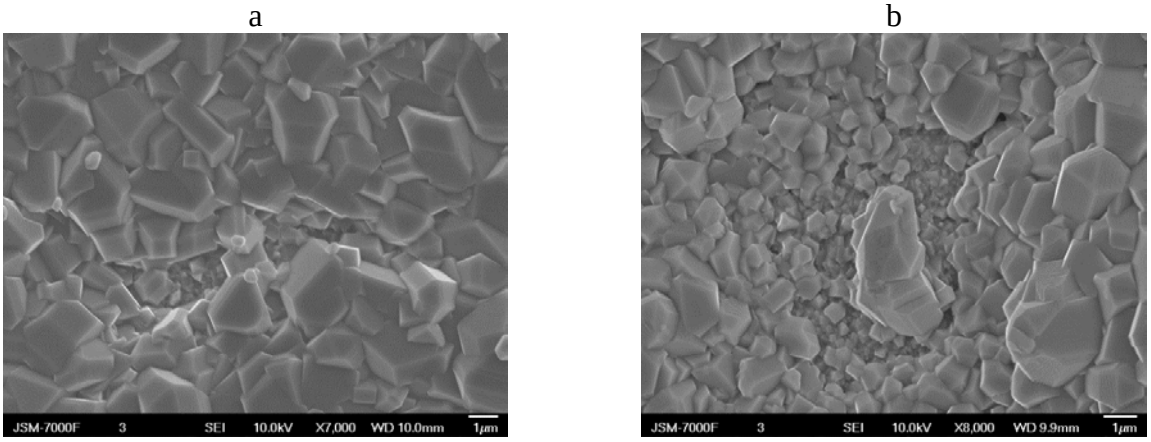

Figure 6. Secondary electron images of the oxide scale (in plan view) formed on the exposed (a) as-received material and (b) thermally-aged material.

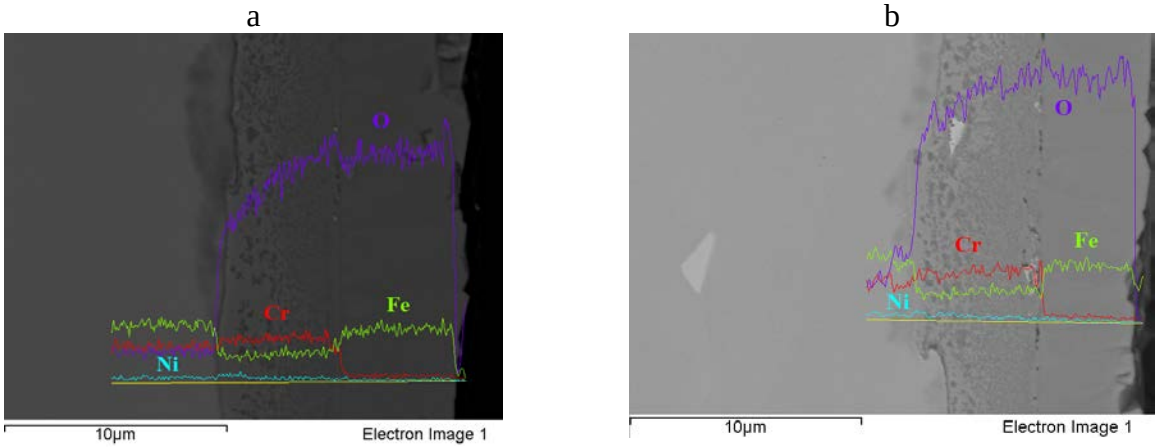

Figure 7. EDS line analysis across the oxide scale/alloy interface of the exposed (a) as-received material and (b) thermally-aged material.

Tan et al. [17] attempted to qualitatively assess the compactness (protectiveness) of the various layers formed on Alloy 800H exposed in SCW by calculating the ratio of the maximum thickness of the layer to the average thickness of the layer, as measured using image analysis. They argued that a ratio approaching unity suggested better coverage and integrity of the oxide layer, and thus better protection. In contrast, a ratio far removed from unity suggested otherwise. A similar analysis (ImageJ software) was performed on the exposed samples in the as-received and thermally-aged condition using the images of the oxide scales shown in Figure 7. The results of the oxide scale thickness measurements are shown in Table 3. The oxide scale formed on both

samples had a similar average total thickness of about 8 μm. Although the average thicknesses of the outer and inner layer formed on the thermally-aged sample were respectively somewhat higher and lower relative to those formed on the as-received material, they were within the range of the error (standard deviation) associated with the as-received sample. The calculated d_{max}/d_{ave} ratio was found to range from 1.4 to 1.8, regardless of the material (as-received vs. thermally-aged) on which the oxide scale formed. This suggests that thermal ageing did not have a marked effect on the protective ability of either the inner or outer oxide layer formed when considering the surface as a whole.

Table 3 Summary of oxide scale thickness measurements.

Condition	Oxide Scale	Maximum Thickness d_{max} (μm)	Average Thickness d_{ave} (μm)	Standard Deviation d_{ave} (μm)	Ratio d_{max}/d_{ave}
As-Received	Total	12.4	8.2	1.8	1.5
	Outer Layer	5.6	4.0	0.7	1.4
	Inner Layer	7.6	4.2	1.2	1.8
Thermally-Aged	Total	11.9	8.0	2.8	1.5
	Outer Layer	6.4	4.5	1.0	1.4
	Inner Layer	6.0	3.5	1.9	1.7

Figure 8 shows a secondary electron image of an intermetallic precipitate embedded at the oxide scale/alloy interface of an exposed thermally-aged sample. Superimposed onto the image is the corresponding EDS (SEM) line scan conducted across both the intermetallic precipitate and the oxide scale/alloy interface. Of particular interest is the significantly reduced thickness of the inner layer that was found to reside on top of the intermetallic precipitate. This finding suggests that the intermetallic precipitates can locally affect the oxide scale formation. This effect was found to depend on the size of the intermetallic precipitate: with the smaller ones tending to be incorporated into the inner layer as it grew. A more detailed examination of this interesting effect is being conducted using TEM of site-specific thin foils prepared using focused ion beam (FIB) milling.

4. Discussion

Thermal ageing for 1000 h at 815 °C was designed to precipitate all of the major phases: carbids, η, χ and σ phases. Of these major phases, the χ and σ phases were significantly more prevalent in the microstructure. Possible reasons for the lower than expected amount of the $M_{23}C_6$ and η phases include: (i) low carbon content, (ii) high ageing temperature, and (iii) residual cold work in the as-received condition (about 15% based on microhardness measurements). All three factors tend to enhance the formation of χ and σ phases [12]. The nucleation and growth of the η phase tends to be weakened when in competition with the nucleation and growth of the χ and σ phases [12]. In terms of the degraded microstructure, the most significant finding is the absence of any depletion in the Cr content found adjacent to the intermetallic precipitates that formed both in the grains and on the grain boundaries, as shown in Fig. 3(b). As already mentioned, this suggests that the expected maximum operating temperature of the fuel cladding (Canadian

SCWR concept) is sufficient allow a “self-healing” of elemental concentration profiles across the various precipitate/matrix phases present in the microstructure that formed as a consequence of thermal ageing.

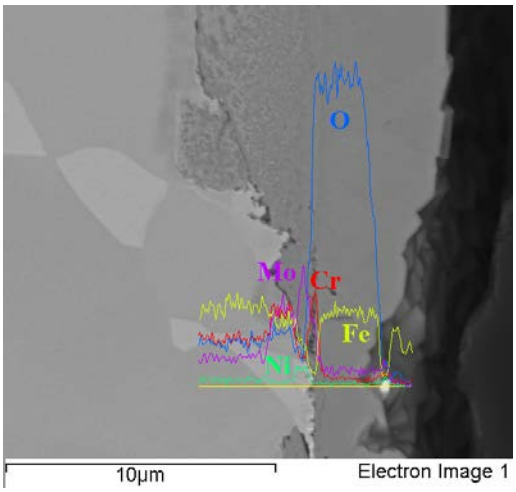

Figure 8. Secondary electron image of intermetallic precipitate embedded at the oxide scale/alloy interface of an exposed thermally-aged sample.

The thermally-aged microstructure of Type 316L stainless steel exhibited essentially the same weight gain and oxide scale structure, chemistry and thickness as the as-received microstructure exposure in 25 MPa SCW at 550 °C for 500 h. This suggests that the formation of intermetallic precipitates had no marked effect on the general (surface area normalized) corrosion resistance. The discontinuous network of Cr-binding intermetallic precipitates both in the grains and on the grain boundaries is believed to be responsible for the absence of any effect. It is generally accepted that the scale growth involves the following simplified steps [18]: (i) nucleation of chromia (Cr_2O_3) precipitates, (ii) reaction of Cr_2O_3 precipitates with Fe and O to form a continuous $FeCr_2O_4$ layer and (iii) diffusion of Fe through continuous $FeCr_2O_4$ layer to form a continuous Fe_3O_4 outer layer. Step (i) requires the diffusion of Cr, which tends to be enhanced along short-circuit paths such as grain boundaries and dislocations lines. The formation of intermetallic particles during thermal ageing has the potential to dramatically affect this process in two ways: binding alloyed Cr and physically blocking the short-circuit paths since these are preferred precipitate nucleation sites [18]. It seems plausible that such a detrimental effect can only be realized if there was a continuous network of precipitates formed on the short circuit diffusion paths. As shown in the set of images presented, this clearly was not the case in the current study. The formation of a continuous network is also unlikely on service (about 30,000 h) based on published predictions of precipitate volume fractions formed after prolonged exposure times (up to 100,000 h at 700 ºC) [19].

Relatively large intermetallic precipitates formed at the oxide scale/alloy interface were observed to significantly reduce the thickness of the inner $FeCr_2O_4$ layer residing directly on top of it. This suggests that the intermetallic precipitates themselves have a higher corrosion resistance relative

to the alloy matrix. The χ and σ phases were more prevalent in the microstructure. Both of these phases have a Cr content of about 50 wt.%. It is well known in high temperature oxidation that a Cr content in excess of 25 wt.% tends to promote the formation of a single Cr_2O_3 layer oxide scale on Fe-based alloys [18]. Therefore, it is believed that the intermetallic precipitates exposed at the oxide scale/alloy interface oxidized to form a thin protective Cr_2O_3 scale on the surface. This thin protective scale was then effective in reducing the amount of Fe available for a subsequent reaction with Cr_2O_3 and O to $FeCr_2O_4$. A detailed TEM examination of the oxide scale/intermetallic precipitate interface is currently underway to better understand the cause of the localized reduction in the inner $FeCr_2O_4$ layer. If true, then the improved corrosion resistance exhibited by the χ and σ phases may in principle be exploited to improve the corrosion resistance of the Type 316L stainless steel if it were somehow present as a continuous layer on the surface.

5. Conclusion

- Thermal ageing for 1000 h at 815 °C (close to the maximum expected fuel cladding temperature in the Canadian SCWR concept) was sufficient to form all of the major intermetallic phases predicted by published time-temperature-precipitation diagrams for Type 316L stainless steel: namely the $M_{23}C_6$, χ, η and σ phases.
- TEM-EDS revealed that there was no significant Cr concentration profiles developed across precipitate/phase boundaries found with the grains or on the grain boundaries. This suggests that Cr diffusion within the microstructure is sufficient at the exposure temperature to avoid sensitized microstructure.
- The thermally-aged material exhibited essentially the same weight gain and oxide scale structure, chemistry and thickness as the as-received material after exposure in 25 MPa SCW at 550 °C for 500 h. This, along with published predictions of precipitate volume fractions after 100,000 h, suggests that the formation of intermetallic precipitates during service is not likely to have a marked effect on the general corrosion resistance (ignoring irradiation effects). The discontinuous network of Cr-binding intermetallic precipitates both in the grains and on the grain boundaries is believed to be responsible for the absence of any effect. The potential effect on stress corrosion cracking is under investigation.
- Relatively large intermetallic precipitates embedded at the oxide scale/alloy interface were observed to significantly reduce the thickness of the inner $FeCr_2O_4$ layer residing directly on top of it. This suggests that the intermetallic precipitates themselves have a higher corrosion resistance relative to the alloy matrix.

6. Acknowledgements

Funding to Canada Gen-IV National Program was provided by Natural Resources Canada through the Office of Energy Research and Development, Atomic Energy of Canada Limited, and Natural Sciences and Engineering Research Council of Canada. The expertise provided by the technical staff at CanmetMATERIALS and the Canadian Centre for Electron Microscopy at McMaster University is greatly appreciated for assisting with the SCW corrosion testing and sample characterization respectively.

7. References

[1]. G.S. Was and T.R. Allen, "Time, temperature, and dissolved oxygen dependence of oxidation of austenitic and ferritic-martensitic alloys in supercritical water", Proceeding of ICAPP'05, Seoul, Korea, 2005, May 15-19.

[2]. G.S. Was, S. Teysseyre and Z. Jiao, "Corrosion of austenitic stainless steel in supercritical water", *Corrosion*, 62, 2006, p. 989.

[3]. S. Teysseyre and G.S. Was, "Stress corrosion cracking of austenitic alloys in supercritical water", *Corrosion*, 62, 2006, p. 1100.

[4]. G.S. Was, R. Ampornrat, G. Gupta, S. Teysseyre, E.A. West, T.R. Allen, K. Sridharan, L. Tan, Y. Chen, X. Ren and C. Pister, "Corrosion and stress corrosion cracking in supercritical water", *Journal of Nuclear Materials*, 371, 2007, p. 176.

[5]. D.A. Guzonas, "Materials and chemistry for a supercritical water-cooled reactor – progress and challenges", Proceedings of the 5th International Symposium on Supercritical Water-Cooled Reactors, Vancouver, BC, Canada, 2011, March 13-16.

[6]. J. Kaneda, S. Kasahara, F. Kano, N. Saito, T. Shikama and H. Matsui, "Material development for supercritical water-cooled reactor", Proceedings of 5th International Symposium on Supercritical Water-Cooled Reactors, Vancouver, BC, Canada, 2011, March 13-16.

[7]. D.A. Guzonas and W.G. Cook, "Cycle chemistry and its effect on materials in a supercritical water-cooled reactor: a synthesis of current understanding", *Corrosion Science*, 65, 2012, p. 48.

[8] I.M. Svishchev, R.A. Carvajal-Ortiz, I. Kashif, I. Choudhry and D.A. Guzonas, "Corrosion behavior of stainless steel 316 in sub- and supercritical aqueous environments: Effect of LiOH additions", *Corrosion Science*, 72, 2013, p. 20.

[9]. W.E. Ruther, R.R. Schlueter, R.H. Lee and R.K. Hart, "Corrosion behavior of steels and nickel alloys in superheated steam," NACE Corrosion Conference Series, Houston, TX, 1965.

[10]. J. Li, W. Zheng, W. Cook, D. Guzonas, S. Penttila, P. Liu and D. Bibby, "Effect of coating and surface modification on the corrosion resistance of selected alloys in supercritical water", Proceedings of 32nd Annual CNS Conference, Niagara Falls, ON, Canada, 2011, June 5-8.

[11]. Y. Tsuchiya, F. Kano, N. Saito, M. Ookawa, J. Kaneda and N. Hara, "Corrosion and SCC properties of fine grain stainless steel in subcritical and supercritical pure water", CORROSION/07, Nashville, TN, U.S.A., 2007, March 11-15.

[12]. B. Weiss and R. Stickler, "Phase instabilities during high temperature exposure of 316 austenitic stainless steel", *Metallurgical Transactions*, 3, 1972, p. 851.

[13]. J.E. Spruiell, J.A. Scott, C.S. Ary and R.L. Hardin, "Microstructural stability of thermal-mechanically pretreated type 316 austenitic stainless steel", *Metallurgical Transactions*, 4, 1973, p. 1533.

[14]. J.K.L. Lai, "A study of precipitation in AISI type 316 stainless steel", *Materials Science and Engineering*, 58, 1983, p. 195.

[15]. T. Sourmail, “Precipitation in creep resistant austenitic stainless steels”, *Materials Science and Technology*, 17, 2011, p. 1.

[16]. A. Kriaa, N. Hamdi and H. Sidhom, “Assessment of intergranular corrosion of heat treated austenitic stainless steel (AISI 316L grade) by electron microscopy and electrochemical tests,” *Protection of Metals*, 44, 2008, p. 506.

[17] L. Tan, T.R. Allen and Y. Yang, “Corrosion behavior of alloy 800H (Fe–21Cr–32Ni) in supercritical water”, *Corrosion Science*, 53, 2011, p. 703.

[18] D. Young, "High temperature oxidation and corrosion of metals", Elsevier Corrosion Series, First edition, Vol. 1, T. Burstein, Editor, Elsevier, Oxford, UK, 2008.

[19] T. Sourmail, H.K.D.H. “Bhadeshia, Modelling simultaneous precipitation reactions in austenitic stainless steels”, *Computer Coupling of Phase Diagrams and Thermochemistry*, 27, 2003, p. 169.

[20] Y. Katayama, M. Tsubota and Y. Saito, “Combination of cold work and heat treatment on stress corrosion cracking susceptibility of L-grade stainless steel” NACE Corrosion Conference Series, Houston, TX, 2003.